Commonly Used Porous Building Materials: Geomorphic Pore Structure and Fluid Transport

Liang Bo Hu, A.M.ASCE[1]; Cabot Savidge[2]; Donna M. Rizzo[3]; Nancy Hayden, M.ASCE[4]; James W. Hagadorn[5]; and Mandar Dewoolkar, M.ASCE[6]

Abstract: Knowledge of microscopic geomorphic structures is critical to understanding transport processes in porous building materials. X-ray scans were obtained of a variety of commonly used porous building materials to both qualitatively and quantitatively evaluate their pore structures. The specimens included natural materials (two sandstones and a limestone) and engineered materials (three types of concretes and a brick). Scanned images were processed to reconstruct the geomorphic structures of these materials. Random walk analyses were performed on the reconstructed pore structures to estimate macroscopic transport properties (including tortuosity, specific surface, and permeability). The effective porosity and permeability of these materials were also experimentally determined and compared to computed values. Calibration of the threshold pixel value used in the postprocessing of X-ray images against measured effective porosity appears to be a more appropriate method of selecting this value than the typical approach, which employs selection based solely on observed histograms. The resulting permeabilities computed by using a calibrated threshold pixel value compare better with the measured permeabilities. This study also demonstrates that the relatively homogeneous and heterogeneous pore structures associated with the natural and engineered building materials under investigation can be captured by X-ray tomography. **DOI: 10.1061/(ASCE)MT.1943-5533.0000706.** © *2013 American Society of Civil Engineers.*

CE Database subject headings: Porous media; Construction materials; Permeability.

Author keywords: Porous building materials; X-ray; Computed tomography; Transport; Permeability.

Introduction

The characterization of geomorphic pore structures (e.g., pore size, shape, and connectivity) of natural and engineered building materials is important for studies of the transport, fate, and remediation of chemical and biological contaminants. It is also of great practical importance to understand the relationship between the geomorphic pore structures and the material properties relevant to fluid transport within them. Although transport in porous media has been intensively investigated in the context of multiphase flow theory, many models are still empirical and involve parameters that are difficult to determine (Richards 1931; Brooks and Corey 1964). Each flow is driven by a pressure gradient; saturation dependent capillary pressure functions and relative permeability functions are needed to solve the system equations. Such models are often further reduced to a nonlinear diffusion equation for the process of unsaturated flow of the wetting fluid in rigid porous building materials (Hall and Hoff 2002; Lockington and Parlange 2003; El Abd et al. 2005). These models usually involve nonlinear diffusivities that depend on saturation. Despite their merits and limitations, all of these approaches require the quantitative characterization of pore structures to understand and model the transport process in porous media. Although traditional macroscopic laboratory experiments can provide average estimates for properties such as porosity, many pore structure details cannot be easily obtained with these methods. In addition, the heterogeneity of pore structures plays a prominent role in the transport process, and therefore, quantifying this property field is an emerging need.

Microfocus X-ray computed tomography has widely been used in a variety of scientific research and engineering studies to obtain three-dimensional (3D) images of opaque materials (White et al. 2006). This technique allows the reconstruction of the porous material microstructure to characterize and quantify the geomorphic structure by image analysis of a series of X-ray scans. In multiphase transport processes, it has emerged as an effective tool for the direct detection of phase evolution (Cnudde and Jacobs 2004; Roels and Carmeliet 2006) and for entities that are difficult to evaluate, such as interfacial surface area and common phase curves (Willson et al. 2004; Zhao and Ioannidis 2007). Nonetheless, effective estimation methods for macroscopic transport properties, including permeability and diffusivity, are still of great interest in many fields such as geophysics, geology, and civil and environmental engineering. Many simulation methods have focused on the determination of the diffusion coefficient and permeability. Coker et al. (1996) extracted several different correlation functions to statistically characterize the pore space morphology and relevant pore space length and time scales from the X-ray image

[1]Assistant Professor, Dept. of Civil Engineering, Univ. of Toledo, 2801 West Bancroft St., Toledo, OH 43606 (corresponding author). E-mail: Liangbo.Hu@utoledo.edu

[2]Engineer, New England Research, Inc., 331 Olcott Dr., Suite L1, White River Junction, VT 05001. E-mail: csavidge@ner.com

[3]Professor, Univ. of Vermont, 33 Colchester Ave., Burlington, VT 05405. E-mail: Donna.Rizzo@uvm.edu

[4]Professor, Univ. of Vermont, 33 Colchester Ave., Burlington, VT 05405. E-mail: Nancy.Hayden@uvm.edu

[5]Tim and Kathryn Ryan Curator of Geology, Denver Museum of Nature and Science, 2001 Colorado Blvd., Denver, CO 80205. E-mail: Whitey.Hagadorn@dmns.org

[6]Associate Professor, Univ. of Vermont, 33 Colchester Ave., Burlington, VT 05405. E-mail: Mandar.Dewoolkar@uvm.edu

Note. This manuscript was submitted on December 30, 2011; approved on October 2, 2012; published online on October 4, 2012. Discussion period open until May 1, 2014; separate discussions must be submitted for individual papers. This paper is part of the ***Journal of Materials in Civil Engineering***, Vol. 25, No. 12, December 1, 2013. © ASCE, ISSN 0899-1561/2013/12-1803-1812/$25.00.

of a Fontainebleau sandstone sample. Similarly, in the Lattice Boltzmann method (Maier et al. 1998; O'Connor and Fredrich 1999; Fredrich et al. 2006), the discrete Boltzmann equation is solved to simulate the flow of a Newtonian fluid and the permeability is obtained through the correlation between the pressure field and the flow velocity field (White et al. 2006). Manwart et al. (2002) and Piller et al. (2009) used a conventional computational fluid dynamics approach to obtain the permeability tensor for a laminar flow through porous media. A possible alternative method proposed by Nakashima and Watanabe (2002), which is relatively easy to implement computationally, uses a random walk algorithm to estimate relevant transport properties. This technique can be used to simulate the Brownian motion of a molecule as it travels in a liquid or a gas, and thus, allows for the extraction of the diffusive properties of the particle in the medium.

One important aspect, when employing the preceding X-ray image analysis, is its applicability in commonly used porous building materials. In combination with several of the computed tomography (CT) scanning technical factors, the complex and possibly heterogeneous material structure presents a challenge for estimating macroscopic transport properties with acceptable levels of accuracy. This paper quantifies the geomorphic pore structures of various natural and engineered porous building materials by using X-ray CT. Similar methods have been applied only to artificial porous systems [e.g., an assembly of beads in the study by Nakashima and Watanabe (2002)] and certain cementitious materials [e.g., cement paste in the study by Promentilla et al. (2009)]. In this work, a variety of natural and engineered building materials including sandstones, limestones, bricks, and concretes were investigated and their transport properties were estimated. X-ray CT was employed to reconstruct the geomorphic pore structure of the materials. The reconstructed geomorphic pore structure was subsequently used to estimate the transport properties. This was achieved by using a random walk-based model. The estimated permeabilities were compared with experimental measurements. Whereas the conventional segmentation processes typically involve an empirical determination of the threshold pixel values based solely on observed histograms, an alternative method based on calibration against experimentally measured effective porosity was also used in the present work. One of the principal goals of this study was to investigate the effects resulting from this calibration on the estimation of other transport properties.

Methods

Materials and Experimental Setup

A variety of natural and engineered building materials were investigated, including three types of concretes, two types of sandstone, one limestone, and one brick. The concrete included: (1) 3,000 psi concrete, produced according to a standard mixing procedure (Derucher et al. 1994) to have a compressive strength of 3,000 psi; (2) 5,000 psi concrete, produced to have a compressive strength of 5,000 psi; and (3) D04 concrete, supplied by Edgewood Chemical Biological Center (ECBC), Maryland. The stone building materials included a sample of arenitic sandstone, hereafter termed "Ohio sandstone," a sample of an arkosic sandstone, hereafter termed "Arkose sandstone," and a sample of a packstone, hereafter termed "Indiana limestone." A generic type of solid brick with sand to granule sized stone aggregate was also obtained from a hardware store for this experiment. Cylindrical core specimens, approximately 12 mm in diameter, were extracted for X-ray CT scanning. As discussed in the subsequent sections, additional smaller and larger Ohio sandstone specimens were used to examine sample size effects. For CT scanning, specimens were cored from the larger specimens used for laboratory macroscopic permeability testing. Because the properties associated with the surfaces of concrete and brick could differ substantially from the properties of their interior, the same interior surface samples were used for both CT scans and macroscopic analyses.

All X-ray scanning was performed with a microfocus X-ray CT scanner (Skyscan 1172). Specimens were scanned at 74 keV (133 μA), with approximately 500–600 equally spaced images collected across 180° of rotation. Three frames were averaged for each image to improve the signal-to-noise ratio; ring artifacts were corrected by using a random movement algorithm; X-ray attenuation slices were generated by using a modified filtered backprojection of shadow images. Resulting stacks of cross-sectional images had voxel size dimensions ranging from 1.5 to 7 μm, depending on the size of the scanned specimens.

Sample X-Ray Images and Image Processing

A typical original cross-sectional X-ray CT image is a grayscale image with pixel values varying from 0 (black) to 255 (white). Shades of gray represent the range of X-ray attenuation through the sample, with black pixels representing the pore space (air) and the white or gray pixels representing the solid phase. A segmentation process is needed to convert the original grayscale image to black and white (B&W) for further analyses. The most common procedure involves the selection of a threshold pixel value. All pixels with values less than the threshold are converted to "0" (black), whereas values above the threshold are converted to "1" (white), resulting in a B&W image. In practice, the colors are often reversed for a more conventional visualization by using black for solids and white for pores.

Selection of the threshold pixel value is a critical factor. It is often selected by using a histogram of pixel values in which two peaks can be identified and distinguished from one another. In practice, most geologic and engineered building materials are comprised of materials whose X-ray contrast are similar and/or overlap one another. In an ideal data set, the minimum point (valley) between the peaks is selected as the threshold (Lu et al. 2006). Alternatively, Nakashima and Watanabe (2002) used the average of these two peak values for the threshold in CT scans of an assembly of beads. In these applications, a clear distinction between glass beads and pores was readily visible prior to any processing; and the two histogram peaks were well separated. However, in scanned images of real building materials, especially cementitious materials, it is often difficult to distinguish the histogram peak values representing the solids and pores, and the separation between the peaks can be very small. As a result, the processing can be quite sensitive to the selection of the threshold. The characteristics of an image are dictated by the physical nature of the porous material, although the processing procedure, quality and limitations of the experimental device, and setup are all potentially significant.

The comparison of pore structure between sandstone and concrete is a good example of this feature. A typical cross-sectional image of an Ohio sandstone specimen is shown in Fig. 1(a) after the contrast is enhanced for a better illustration. The corresponding cropped B&W image [Fig. 1(b)] has colors reversed for more conventional visualization (white pixels representing the pore space). The boundaries of the sandstone grains are distinguishable from the pores. Fig. 2(a) shows an enhanced X-ray portion of a 5,000 psi concrete specimen. It clearly reveals the coarse aggregates (lightest shade of gray) and small pores (darkest gray) between these aggregates. Most of the space between the coarse aggregates may be

J. Mater. Civ. Eng. 2013.25:1803-1812.

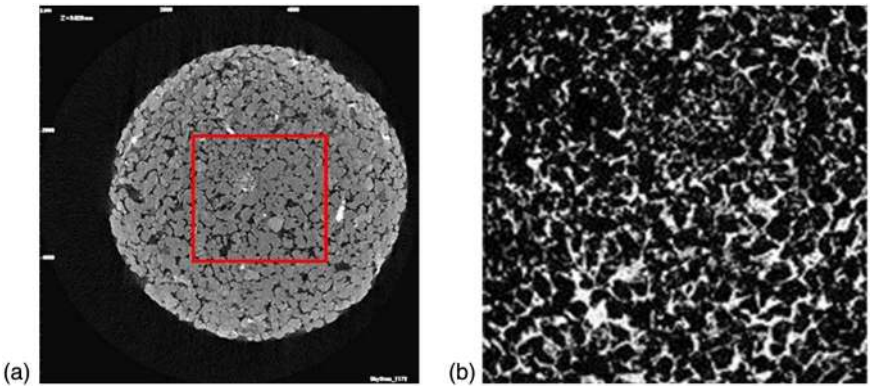

Fig. 1. (a) Enhanced sample X-ray image of an Ohio sandstone specimen (5 × 5 mm in diameter), in which a cropped area is outlined in the square (contrast enhanced); (b) final B&W image after image processing

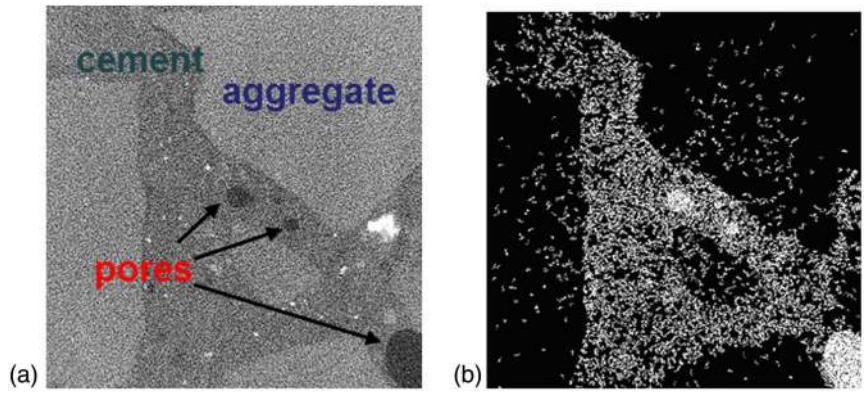

Fig. 2. (a) Enhanced sample X-ray image of a portion of a 5,000 psi concrete specimen; (b) final B&W image after image processing

finer sand to clay sized aggregates or cement. As a result, its final B&W image critically depends on the selected threshold. In this case, the threshold determines the fraction of the pore space among the fine aggregates. The B&W image of Fig. 2(b) has a high selected pixel threshold (25), and therefore a larger porosity. X-ray images of the rest of the investigated materials are provided in Fig. 3.

Quantification of porosity in this case may be obtained directly from the pixel histogram. Fig. 4 shows the histogram of the original X-ray image (Fig. 2) of the 5,000 psi concrete in which most of the pixels have values less than 100. A closer look at the histogram distribution reveals two peaks. The first peak, pixel value 0, represents the pores. The second peak, at approximately 30, has the largest population. Consequently, the selection of a threshold value between 0 and 30 would delineate the pore structure and the porosity. The porosity may be plotted as a function of the selected threshold value (Fig. 5), resulting in the cumulative distribution function of the histogram. Changing the threshold from 15 (the midpoint between 0 and 30) to 20 would result in a difference of almost 0.10 in terms of absolute value of porosity.

Because of this potential discrepancy, it is often recommended to experimentally measure the porosity and adjust the contrast threshold until the porosity (estimated by using the image alone) reasonably matches the measured porosity (Promentilla et al. 2009). This is the approach adopted in this study. The measured porosity is the effective material porosity when the connectivity of the pores has been considered. Therefore, the calculated porosity must be based on those connected pores only, which must be evaluated through 3D reconstruction rather than from a two-dimensional (2D) slice. Computationally, this is achieved by using *MATLAB* (V7.7) functions to identify those connected pores (numerically represented as ones) in a 3D matrix. In this study, both criteria were used for the segmentation process, including: (1) effective porosity calibration-based thresholding, and (2) histogram-based thresholding. In the subsequent section, the transport properties were simulated by using the distinctive pore structures resulting from the different thresholding methods. Comparison between these estimations allows the effectiveness of each method to be assessed.

The 3D material pore structure can subsequently be reconstructed with volume rendering and is useful for simulating the material properties of these commonly used building materials. The memory required to process the 3D matrix is significantly greater than the 2D matrix. As a consequence, the size of the reconstructed 3D volume on which random walk simulations are performed is usually much smaller than the original scanned image. In the present study, a stack of 250 scans are used to generate a 250^3-voxels cube with a size of $\sim(900\ \mu\text{m})^3$, or a little less than 1 mm^3. The selected size of the matrix is close to the upper limit afforded with a conventional PC with 3 GB of RAM. All of the general estimation methods discussed in the following sections are readily applicable to 2D images, which often provide better demonstration examples. All computation was implemented by using *MATLAB* V7.7.

Determination of Porosity and Specific Surface Area

The Ohio sandstone was rather homogeneous even at a relatively small scale; in contrast, the presence and distribution of large

J. Mater. Civ. Eng. 2013.25:1803-1812.

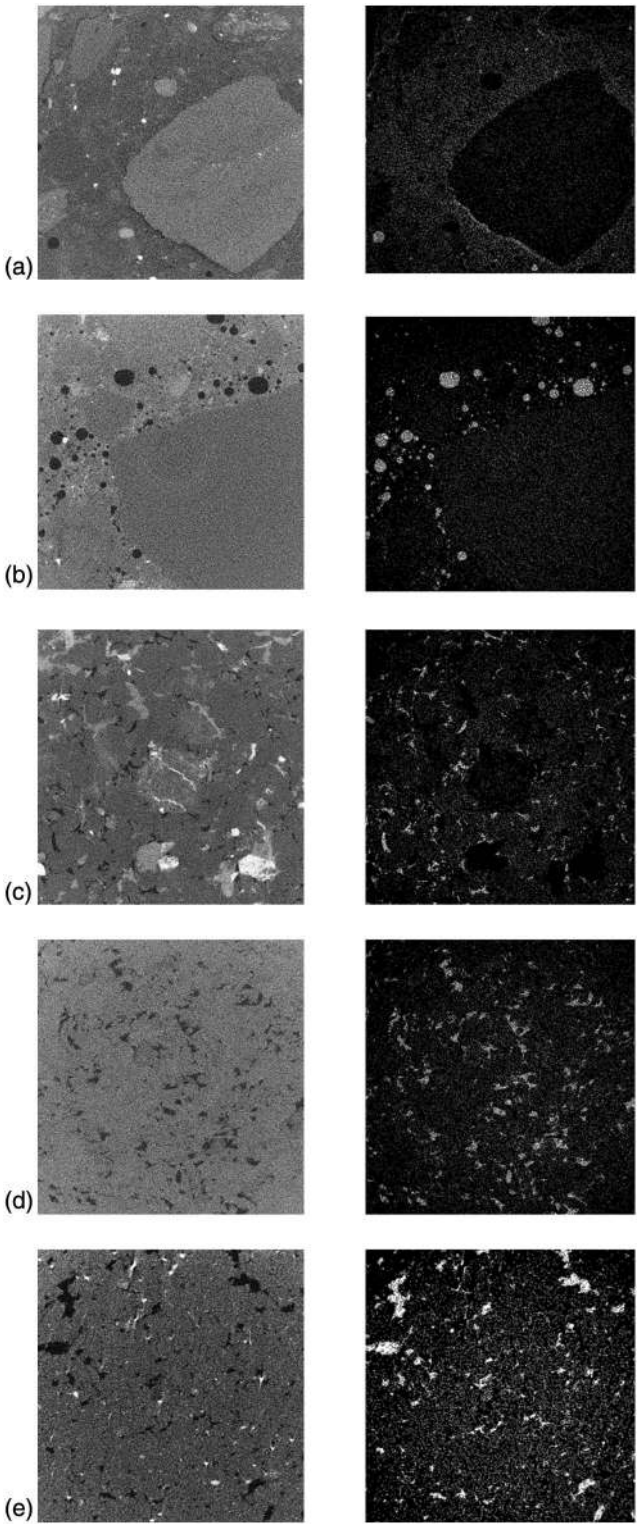

Fig. 3. Portion of an enhanced sample X-ray image (left) and its corresponding B&W image after image processing (right): (a) 3,000 psi concrete; (b) D04 concrete; (c) Arkose sandstone; (d) Indiana limestone; (e) brick

aggregates rendered 5,000 psi concrete inhomogeneous, at least at a macroscopic specimen scale. Quantitatively, two properties that can be directly computed from the X-ray images, porosity and specific surface area, may be used to examine the heterogeneity of the studied materials.

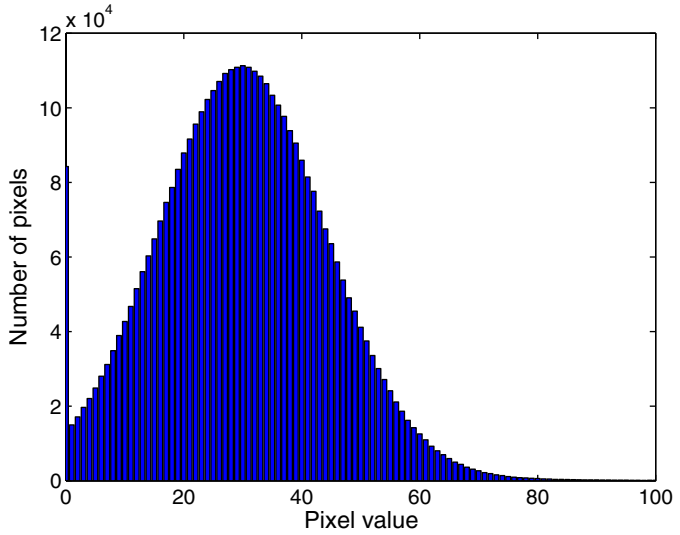

Fig. 4. Histogram of an original scan of 5,000 psi concrete specimen [Fig. 3(a)]

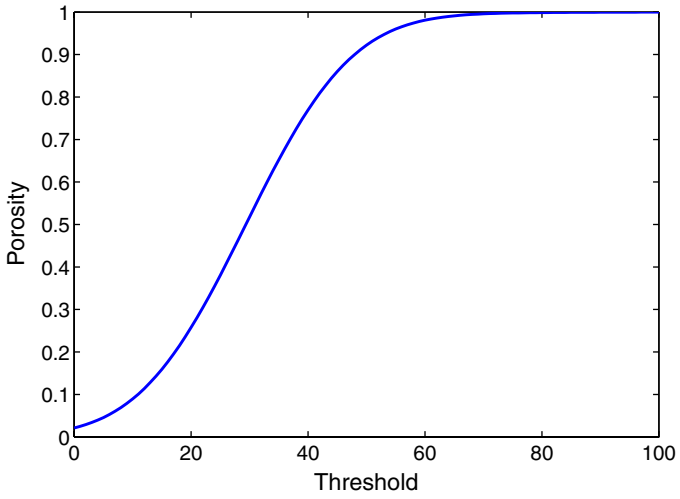

Fig. 5. Total porosity in relation to the selected threshold, i.e., the cumulative function of the histogram in Fig. 4

Porosity may be computed by counting the number of white pixels (ones) in the matrix representing the B&W 2D image, or in the 3D array representing a volume. The specific surface area discussed in this work is defined as the surface area of the solid pore interface per unit total (bulk) volume of porous material, $(S/V)_t$. This quantity is inversely related to the ratio of the surface area of solid pore interface to the volume of pores, termed surface to volume of pores, $(S/V)_p$, by porosity ϕ, $(S/V)_p = 1/\phi(S/V)_t$. The surface to volume of pores may be considered characteristic of the pore size; the specific surface area considered here solely describes the amount of solid pore interface area in a given volume of porous material.

The solid pore interfacial surface area can be directly obtained by identifying solid pore interfaces in a 3D array and calculating the surface area represented. In 2D images, the specific surface area is reduced to the ratio of the perimeter of the solid pore interface to the total area.

The heterogeneous nature of the porous materials studied in this work was evaluated by using the distribution of porosity

J. Mater. Civ. Eng. 2013.25:1803-1812.

and specific surface area. Estimates were obtained based on the histogram-based thresholding. The distribution of porosity and specific surface area in Ohio sandstone and 5,000 psi concrete along the vertical (z) direction of a cylindrical specimen are plotted in Figs. 6 and 7, respectively. At each location along z, 64 estimations are made in a volume of $2{,}000 \times 2{,}000 \times 250$ pixels, which is divided into 8×8 cubes [each cube of 250^3 pixels has a volume of $\sim(900\ \mu\text{m})^3$]. A 250^3-pixel array (cube) was chosen because it is nearly the maximum 3D array size that the computer used in this research can handle, while simultaneously being efficient at running a walker (particle) to produce meaningful random walk simulations. The distributions of porosity and specific surface are more continuous and vary significantly less for Ohio sandstone than 5,000 psi concrete. The average porosity was calculated to be 0.22 with an SD of 0.03 for Ohio sandstone. The average porosity and SD for 5,000 psi concrete were 0.17 and 0.08, respectively. Ohio sandstone also has an average specific surface area of $8.31 \times 10^4\ \text{m}^{-1}$ with an SD of $1.13 \times 10^4\ \text{m}^{-1}$, whereas 5,000 psi concrete has an average specific surface area of $7.96 \times 10^4\ \text{m}^{-1}$ with an SD of $2.88 \times 10^4\ \text{m}^{-1}$. The variation along the cylindrical core of the concrete specimen clearly manifests the heterogeneous nature of concrete.

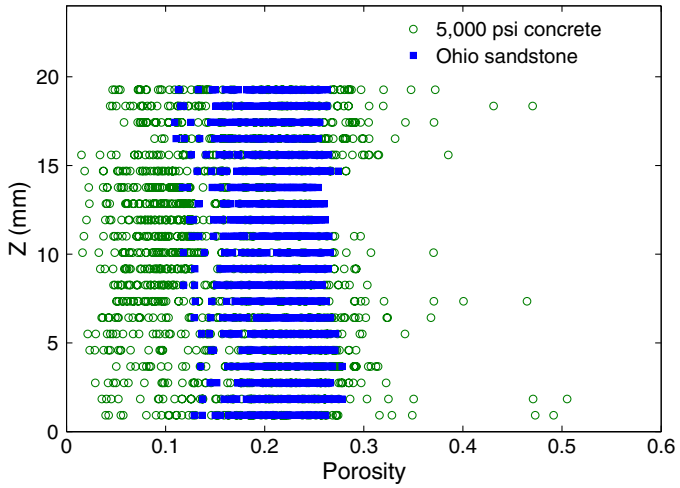

Fig. 6. Porosity profiles for Ohio sandstone and 5,000 psi concrete

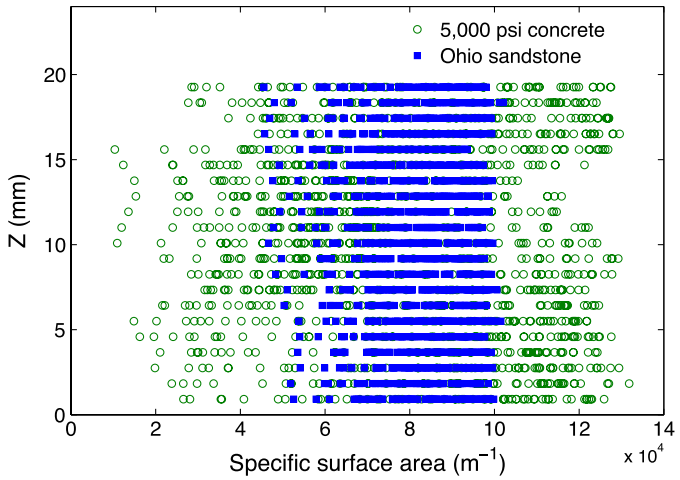

Fig. 7. Specific surface area profiles for Ohio sandstone and 5,000 psi concrete

Estimation of Tortuosity and Permeability

There are several ways to estimate other transport properties such as permeability by using the reconstructed porous structure from the X-ray CT images. Here, the random walk algorithm discussed by Nakashima and Watanabe (2002) was adopted because of its simplicity and relative computational efficiency. The relationship of random walk simulation to the stochastic Wiener process, a process similar to Brownian motion, has been established in probability and statistics theory (Feller 1968). A detailed discussion and review of its correlation to the diffusion coefficient can be found in the studies by Nakashima and Watanabe (2002) and Anta et al. (2008). In the following, a B&W image from one of the CT scans (Fig. 1) is used to illustrate the essential components of this approach. A particle (or walker) is initially placed at random inside a pore (Fig. 8). It subsequently migrates randomly along discrete pixels over time, which is denoted using a dimensionless integer time, τ. Usually, a large number of these particles must be used and the average of the square distances of all of these random particles are computed as mean-square displacement $< r(\tau)^2 >$, as a function of τ. A general 3D formulation may be expressed by the following equation:

$$\begin{aligned} <r(\tau)^2> &= \frac{1}{n}\sum_{i=1}^{n} r_i(\tau)^2 \\ &= \frac{1}{n}\sum_{i=1}^{n}\{[x_i(\tau)-x(0)]^2 + [y_i(\tau)-y(0)]^2 \\ &\quad + [z_i(\tau)-z(0)]^2\} \end{aligned} \tag{1}$$

where x_i, y_i, and z_i = coordinates of the ith particle; and n = number of particles. In 2D cases, only x_i and y_i need to be considered.

If this random walk is completely unrestricted, i.e., in a void without any solid particles present, $< r(\tau)^2 >$ is proportional to τ (solid line in Fig. 9), and the proportionality constant will reflect the diffusion coefficient of the particle in the free space without solids (water diffusivity in bulk water). However, because real porous media contain solids (black pixels in Fig. 8), $< r(\tau)^2 >$ is reduced because the solids act as obstacles. The change in the function $< r(\tau)^2 >$ provides a measure for the diffusivity in real porous materials; thus, tortuosity may be obtained by comparing the gradient to that of a free random walk $< r(\tau)^2 >_{\text{free}}$. According to Nakashima and Kamiya (2007), the geometrical tortuosity may

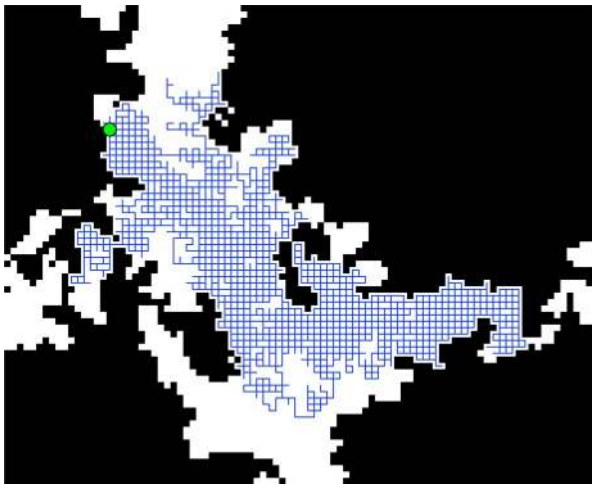

Fig. 8. Sample 2D random walk trajectory in the pore space of Ohio sandstone (the solid circle indicates the initial location of the particle)

J. Mater. Civ. Eng. 2013.25:1803-1812.

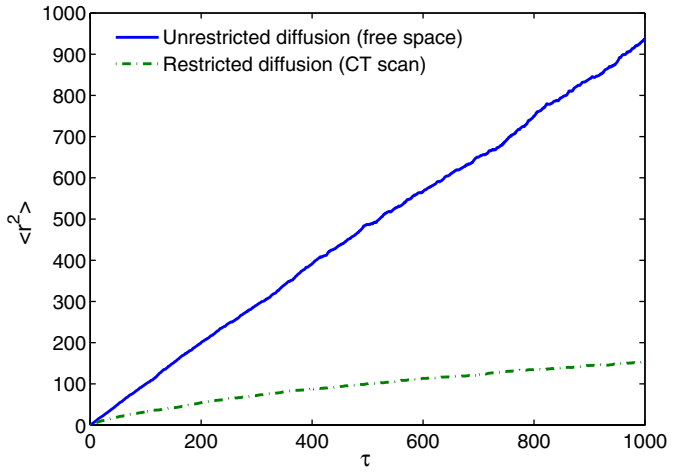

Fig. 9. Mean-square displacement of the random walk for a total of 2,000 particles, as shown in Fig. 8

be represented as the ratio between these gradients, D_0/D, and a useful expression can be obtained:

$$\frac{D}{D_0} = \frac{\frac{dr(\tau)^2}{d\tau}}{a^2} = 1 - \frac{4a}{9\sqrt{6\pi}}\left(\frac{S}{V}\right)_p \sqrt{\tau} + c_2\tau \tag{2}$$

where c_2 = data fitting constant; a = lattice constant of the simple lattice, i.e., the dimension of a CT pixel. This equation can be used to estimate $(S/V)_p$ via data fitting. Furthermore, permeability can also be estimated based on the Kozeny-Carman equation:

$$k = \frac{\alpha\phi}{(\frac{D_0}{D})(\frac{S}{V})_p^2} = \frac{\alpha\phi^3}{(\frac{D_0}{D})(\frac{S}{V})_t^2} \tag{3}$$

where α = correction factor and is often assumed to be 1 when details of the pore geometry are unknown. It was found that $(S/V)_p$ is readily available from the images; therefore, the use of Eq. (2) to obtain the estimates of $(S/V)_p$ is not an absolute necessity, especially when the curve fitting does not yield a satisfactory match for the proposed form of the function. The porosity in the preceding equation is typically the total porosity. In this study, this estimation is also evaluated by replacing the total porosity with the effective porosity in the subsequent sections.

In random walk simulation, the distance a particle travels is confined to the area (for 2D) or the space (for 3D) of the pores. For example, for a 100×100 matrix representing a porous medium in Eq. (1), the maximum possible square displacement for each walker is the longest distance, $100\sqrt{2}$. Consequently, the mean square displacement for all of the walkers is bounded, that is, $<r(\tau)^2>$ will approach an upper limit over time. Even for $<r(\tau)^2>_{\text{free}}$, obtained from simulation in a free space, it can continue to grow proportionally to τ only if the random walk is allowed in an infinite free space. This implies that in computing $<r(\tau)^2>_{\text{free}}$, it is more appropriate to use the free space of the same size instead of an infinite free space.

In addition to the porosity, specific surface area, tortuosity, and permeability, the connected pores may be identified in any given 2D or 3D image. For example, *MATLAB* permits identification of the pixel connectivity, defined according to whether faces (6-connectivity), edges (18-connectivity), or corners (28-connectivity) touch those of adjacent pixels. This capability allows one to obtain the continuous pore space in a 3D cube, whereas the rest of the pore space may be considered isolated. The volume fraction of the connected pores is referred to as the effective porosity (Promentilla et al. 2009), which is more similar to that measured in the laboratory than the total porosity.

Results and Discussion

The aforementioned 3D transport properties for each material were estimated by using the reconstructed porous structure based on two different thresholding criteria, discussed previously. In the simulations based on the calibration-based thresholding criterion, the threshold was adjusted iteratively until the effective porosity matched that measured in the experiments. Subsequently, in the image analysis and random walk simulations, all estimates were based on a volume of $2{,}000 \times 2{,}000 \times 250$ voxels divided into 8×8 cubes, each having 250^3 voxels (0.93 mm^3). The transport properties are estimated for each material and summarized in Table 1. The measured permeability is obtained in the laboratory by using ASTM standard D5084-00 (2002). These tests were performed on specimens of 50 mm in diameter and 50 mm in height. The effective porosity was estimated for the same specimen after its permeability was determined. Each specimen was initially oven dried and weighed. The permeability test was conducted as a continuous water flow was introduced to the specimen for permeability measurement. Subsequently, the specimen was weighed and the weight difference was converted to the volume of water to determine the volume of pore space occupied by water. This porosity was considered to be the effective porosity because it is reasonable to presume that the water only enters the connected pores. For each material, five specimens were tested for both permeability and effective porosity measurements, and the average results are reported here. Simulations were performed in each cube and resulted in 64 estimates that were averaged and reported in Table 1.

In addition to the experimentally measured effective porosity and permeability, Table 1 includes the estimated total porosity,

Table 1. Estimates of Transport Properties with Experimental Effective Porosity-Based Thresholding

Material	Computed porosity (%)	Computed effective porosity (%)	Measured effective porosity (%)	Computed tortuosity	Computed specific surface area (m^{-1})	Computed permeability (ρ-based) (m^2)	Computed permeability (ρ_e-based) (m^2)	Measured permeability (m^2)
Ohio sandstone	15.0	11.1	11.5	6.5	6.3×10^4	1.3×10^{-13}	0.8×10^{-13}	1.4×10^{-13}
Arkose sandstone	13.3	5.8	7.5	9.1	6.5×10^4	7.2×10^{-14}	1.9×10^{-14}	2.1×10^{-14}
Indiana limestone	15.0	7.4	7.5	8.9	7.5×10^4	8.6×10^{-14}	2.6×10^{-14}	6.4×10^{-14}
Brick	33.6	30.0	31.1	3.1	7.4×10^4	1.3×10^{-11}	1.1×10^{-11}	9.2×10^{-13}
D04 concrete	17.4	11.1	11.0	7.7	8.2×10^4	1.4×10^{-13}	6.0×10^{-14}	1.9×10^{-14}
3,000 psi concrete	17.1	11.5	13.2	10.0	8.4×10^4	1.1×10^{-13}	6.6×10^{-14}	4.5×10^{-14}
5,000 psi concrete	20.3	15.9	17.3	11.6	9.5×10^4	2.0×10^{-13}	1.6×10^{-13}	4.2×10^{-14}

J. Mater. Civ. Eng. 2013.25:1803-1812.

effective porosity, tortuosity, specific surface area, and permeability. In essence, the effective porosity was calibrated to the measured porosity by adjusting the threshold pixel value; however, the estimated effective porosity did not exactly match the measured because of the discrete nature of the pixel values. The seventh column shows the permeability estimates via Eq. (3) by using the total porosity (ρ). The differences between the estimated and measured permeability were generally within one order of magnitude for most of the materials, with the exception of brick. This level of accuracy may be regarded as satisfactory, considering the complex geomorphic structures of real building materials, which usually exhibit a wide range for permeability (Savidge 2010). Permeability estimates for the natural and homogeneous materials, sandstones and limestone, were particularly close to the measured values. Among concretes, the differences for 5,000 psi and D04 concretes were greater than the variations for 3,000 psi concrete.

The eighth column in Table 1 shows the permeability estimates via Eq. (3) by using the effective porosity (ρ_e). The difference was not significant, but for cementitious materials, it can be considered a minor improvement. Estimates for brick are also challenging as a result of its heterogeneous nature. The brick sample possessed a large porosity and the simulated permeability was considerably higher than the measurement. Figs. 10 and 11 show the effective porosity field for Ohio sandstone and 3,000 psi concrete, respectively, by using the 64 (8×8) data points and by shading such that each cell is a bilinear interpolation of the values at its four vertices. The 3,000 psi concrete was clearly heterogeneous, with the presence of large aggregates indicated by the near zero effective porosity. Figs. 12 and 13 show the estimated permeability field for Ohio sandstone and 3,000 psi concrete, respectively. The estimates of permeability (in log scale) ranged between −11 and −16 orders of magnitude (Fig. 13). In stark contrast, the homogeneous nature of Ohio sandstone (Fig. 12) showed a very narrow range of the estimated permeability.

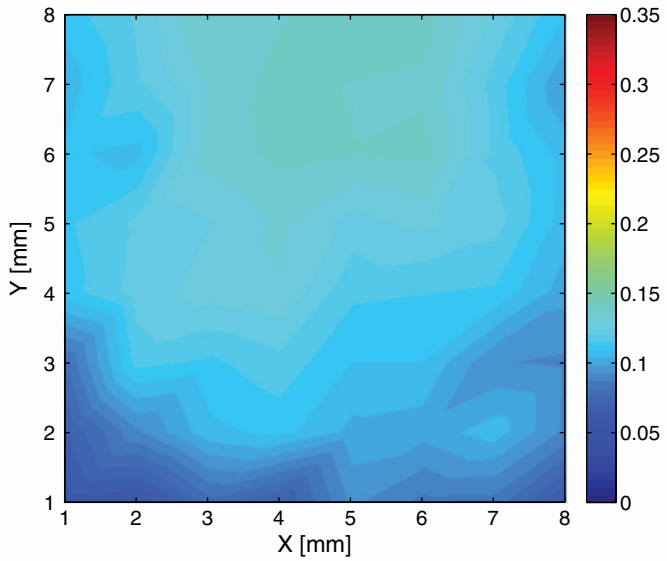

Fig. 10. (Color) Ohio sandstone: effective porosity field

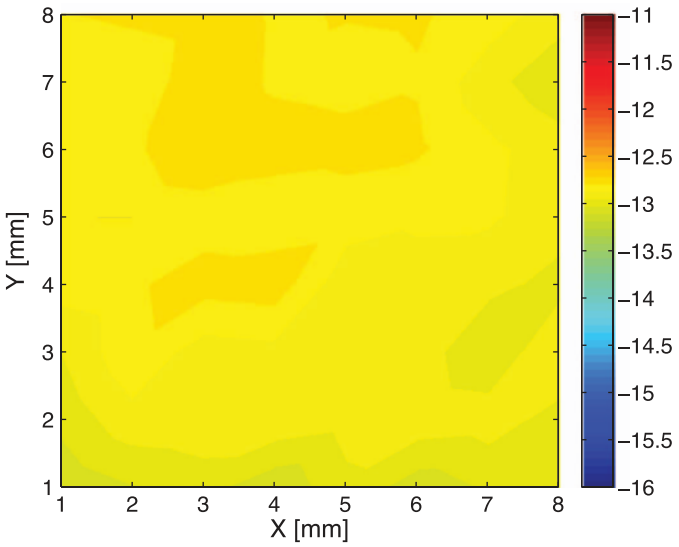

Fig. 12. (Color) Ohio sandstone: estimated permeability field (log m^2)

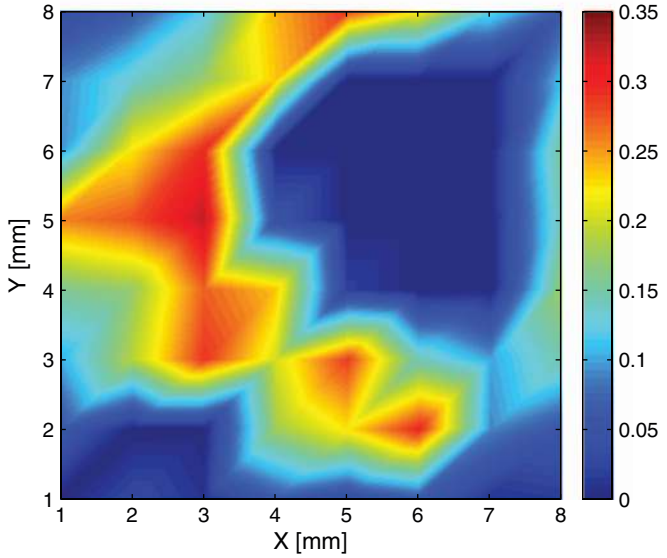

Fig. 11. (Color) 3,000 psi concrete: effective porosity field

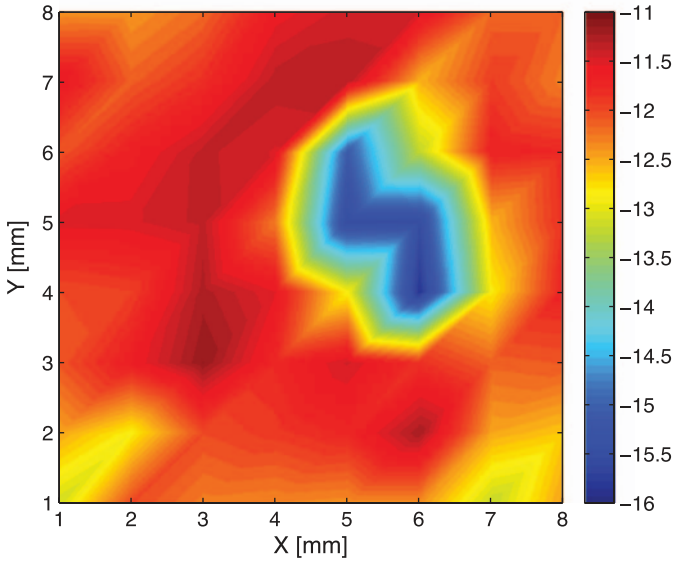

Fig. 13. (Color) 3,000 psi concrete: estimated permeability field (log m^2)

J. Mater. Civ. Eng. 2013.25:1803-1812.

The second criterion examined in this study was to select the threshold between solid and pore based on the histogram using the mean value of the two peaks, as discussed in the preceding section. When the threshold was adjusted to match the porosity measurement, as presented in Table 1, it was expected to yield better estimates of the porosity than histogram-based thresholding; it is interesting to compare the estimates of other transport properties using these two different criteria. The subsequent simulations for these properties followed the same procedure as already outlined after the porous structure was reconstructed. Results are presented in Table 2 and suggest that thresholding based solely on pixel histogram may not result in an accurate estimation for porosity. Especially for the cementitious materials examined herein, ρ_e was very small; as a consequence, the permeability estimated using ρ_e was nearly equal to zero. However, estimates using ρ were sufficiently close, partially because their counterparts based on the first thresholding criterion (Table 1) generally overestimated the permeability; with smaller estimated porosity, estimation for permeability actually improved slightly.

Considering that the seven tested materials may be classified into two categories: natural (sandstone and limestone) and engineered (brick and concrete), a direct comparison can be made between the estimates and the experimental results using the total porosity, ρ (Fig. 14), and the effective porosity, ρ_e (Fig. 15). Comparing the estimates in Fig. 14 with those in Fig. 15, it appears that calibration-based thresholding is more precise than histogram-based thresholding. In general, calibration-based thresholding slightly overestimates the permeabilities, whereas histogram-based thresholding underestimates the permeabilities. For natural materials such as those in this study, both thresholding techniques seem adequate if estimates are made using the total porosity. If the effective porosity is used, calibration-based thresholding provides better estimates for both natural and engineered materials.

Clearly, the purpose of X-ray CT scanning is to reproduce the geomorphic structure of opaque materials as accurately as possible. However, the quality of the original scans can be affected by material composition and X-ray experimental techniques, in addition to the subsequent image processing; such variations may largely dictate the accuracy of the reconstructed material structure, which serves as a basis for further simulations, and consequently, strongly influences the simulation results. Similarly, each simulation method has different stengths and weaknesses as a function of the validity of its assumptions and its specific computational demands; in general, these have a lesser impact than the reconstruction of the material nature. The current numerical analysis indicates the potential necessity of applying multiple segmentation techniques including thresholding, region growing, classifier method, or clustering (Pham et al. 2000) for reliably reconstructing porous materials. Finally, the methodology used to characterize the

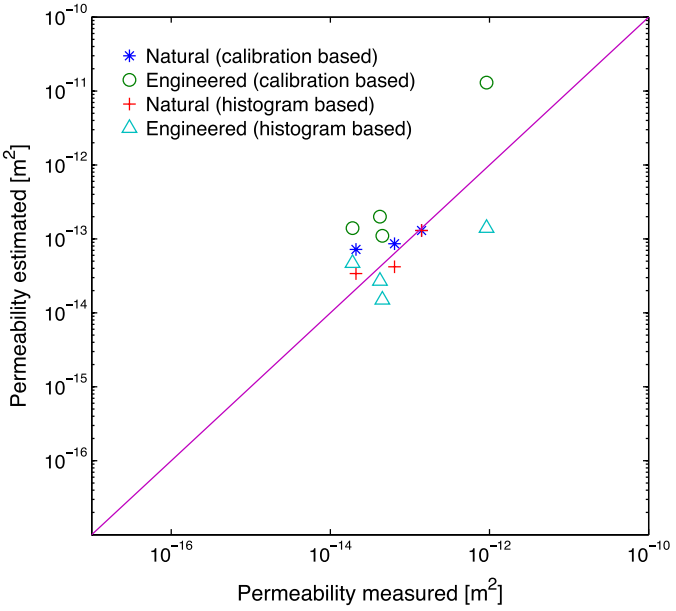

Fig. 14. Permeability, estimated by using ρ versus measured

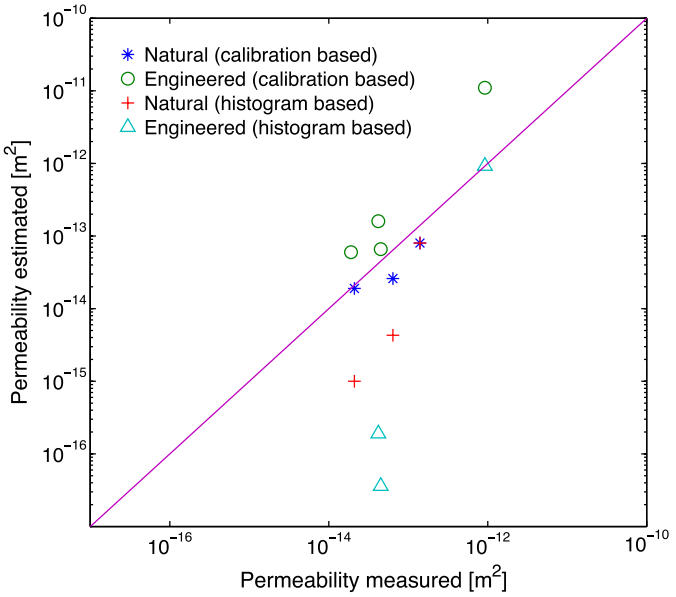

Fig. 15. Permeability, estimated by using ρ_e versus measured

Table 2. Estimates of Transport Properties with Histogram-Based Thresholding

Material	Computed porosity (%)	Computed effective porosity (%)	Measured effective porosity (%)	Computed tortuosity	Computed specific surface area (m^{-1})	Computed permeability (ρ-based) (m^2)	Computed permeability (ρ_e-based) (m^2)	Measured permeability (m^2)
Ohio sandstone	15.0	11.1	11.5	6.5	6.3×10^4	1.3×10^{-13}	1.4×10^{-13}	1.4×10^{-13}
Arkose sandstone	8.9	2.3	7.5	11.5	4.6×10^4	3.4×10^{-14}	1.0×10^{-15}	2.1×10^{-14}
Indiana limestone	10.3	2.3	7.5	11.6	5.4×10^4	4.2×10^{-14}	4.3×10^{-15}	6.4×10^{-14}
Brick	16.7	11.3	31.1	6.0	4.5×10^4	14×10^{-13}	9.2×10^{-13}	9.2×10^{-13}
D04 concrete	8.8	0.0	11.0	15.8	4.6×10^4	4.7×10^{-14}	0	1.9×10^{-14}
3,000 psi concrete	6.7	0.1	13.2	28.6	3.9×10^4	1.5×10^{-14}	3.6×10^{-17}	4.5×10^{-14}
5,000 psi concrete	8.3	0.5	17.3	44.6	4.6×10^4	2.7×10^{-14}	1.9×10^{-16}	4.2×10^{-14}

J. Mater. Civ. Eng. 2013.25:1803-1812.

Table 3. Parameters Estimated for Ohio Sandstone of Different Sizes

Resolution (μm)	1.5	3.67	6.27
Sample diameter (mm)	5	12.5	24
Porosity (%)	11.5	11.2	11.8
Tortuosity	4.6	21.6	58.3
Specific surface area (m^{-1})	4.5×10^4	2.8×10^4	4.0×10^4
Permeability (m^2)	21×10^{-14}	8.1×10^{-14}	1.8×10^{-14}

materials of concern also depends on the associated scale of the primary observations relative to the grain or aggregate size of the studied materials, especially when localized estimates are not adequate for field level or macro scale characterizations.

Because the scan system employed in these experiments has a fixed field of view (4,000 × 4,000 pixels for a slice), the resolution of the image pixels depends on the sample size of the specimen. To explore the effects of resolution on the property estimates, three Ohio sandstone cores with diameters of 5, 12.6, and 24 mm, corresponding to X-ray spatial resolutions of 1.5, 3.67, and 6.27 μm, respectively, were scanned to generate identically sized images (4,000 × 4,000 pixels). Thresholds were selected to match the measured porosity, and subsequently, the other properties were obtained (a summary is provided in Table 3).

The wide range of tortuosity values computed from the random walk suggests that coarser resolution (i.e., larger mean voxel size) tends to be inadequate when detecting possible connected pores. This effect was also reported in the study by Promentilla et al. (2009), in which the results are based on images (matrices) of different sizes representing the same specimen. The results of specific surface area did not show a monotonic correlation with the resolution, partially because the porosity was nearly identical and did not reflect an effect on the pore connectivity. The permeability estimates in this case were mostly affected by the difference in tortuosity estimates and were understandably greater for finer resolution, smaller sized voxel dimensions.

Conclusions

Seven commonly used porous building materials were examined by using X-ray CT. The materials included three seemingly homogeneous natural stones (two sandstones and a limestone) and four heterogeneous engineered materials (three concretes and a brick). Scanned images of each building material were processed to reconstruct their geomorphic structures and two approaches were examined for thresholding in the analysis of these samples. Random walk simulations were performed on the reconstructed pore structures to compute properties that are relevant to transport phenomena, such as tortuosity, specific surface, and permeability. The computed porosities and permeabilities were compared to the measured values.

The calibration-based method for permeability analysis seemed to provide better estimates than the histogram-based method, especially when the effective porosity was used in Eq. (3). Presently, the latter is more commonly used, but may not be appropriate for cementitious and heterogeneous building materials such as concrete and brick. The reconstructed geomorphic structures of these heterogeneous engineered materials varied greatly when the thresholds for image analysis were selected based on the histograms.

Measured and computed permeabilities were generally within one order of magnitude of each other when the thresholding was based on measured effective porosity. The computed permeabilities compared better with the measured permeabilities when the thresholding was based on the measured effective porosity than the histogram, particularly for the heterogeneous, artificial materials.

Finally, the relatively homogeneous and heterogeneous pore structures of commonly used natural and engineered building materials can be captured by X-ray tomography.

Acknowledgments

Support for this work was provided by Defense Threat Reduction Agency, HDTRA1- 08-C-0021. We thank Ms. Lindsay Meador for help in the laboratory.

References

Anta, J. A., Mora-Sero, I., Dittrichc, T., and Bisquert, J. (2008). "Interpretation of diffusion coefficients in nanostructured materials from random walk numerical simulation." *Phys. Chem. Chem. Phys.*, 10(30), 4478–4485.

ASTM. (2002). "Soil and rock; building stones." *D5084-00*, West Conshohocken, PA.

Brooks, R. H., and Corey, A. T. (1964). "Hydraulic properties of porous media." *Hydrology papers*, Colorado State University, Fort Collins, CO.

Cnudde, V., and Jacobs, P. J. S. (2004). "Monitoring of weathering and conservation of building materials through non-destructive x-ray computed microtomography." *Environ. Geol.*, 46(3–4), 477–485.

Coker, D. A., Torquato, S., and Dunsmuir, J. H. (1996). "Morphology and physical properties of Fontainebleau sandstone via a tomographic analysis." *J. Geophys. Res.*, 101(B8), 17497–17506.

Derucher, K., Korfiatis, G., and Ezeldin, A. (1994). *Materials for civil and highway engineers*, 3rd Ed., Prentice Hall, NJ.

El Abd, A. E. G., Czachor, A., Milczarek, J. J., and Pogorzelski, J. (2005). "Neutron radiography studies of water migration in construction porous materials." *IEEE Trans. Nucl. Sci.*, 52(1), 299–304.

Feller, W. (1968). *An introduction to probability theory and its applications*, Wiley, New York.

Fredrich, J. D., DiGiovanni, A. A., and Noble, D. R. (2006). "Predicting macroscopic transport properties using microscopic image data." *J. Geophys. Res.*, 111(B3), B03201.

Hall, C., and Hoff, W. W. (2002). *Water transport in bricks, stones and concrete*, Spon Press, New York.

Lockington, D. A., and Parlange, J. Y. (2003). "Anomalous water absorption in porous materials." *J. Phys. D*, 36(6), 760–767.

Lu, S., Landis, E. N., and Keane, D. T. (2006). "X-ray microtomographic studies of pore structure and permeability in portland cement concrete." *Mater. Struct.*, 39(6), 611–620.

Maier, R. S., Kroll, D. M., Kutsovsky, Y. E., Davis, H. T., and Bernard, R. S. (1998). "Simulation of flow through bead packs using the lattice boltzmann method." *Phys. Fluids*, 10(1), 60–74.

Manwart, C., Aaltosalmi, U., Koponen, A., Hilfer, R., and Timoten, J. (2002). "Lattice-boltzmann and finite-difference simulations for the permeability for three-dimensional porous media." *Phys. Rev. E*, 66(1), 016702.1–016702.11.

MATLAB, V7.7 [Computer software]. MathWorks, Inc., Natick, MA.

Nakashima, Y., and Kamiya, S. (2007). "Mathematica programs for the analysis of three-dimensional pore connectivity and anisotropic tortuosity of porous rocks using x-ray computed tomography image data." *J. Nucl. Sci. Technol.*, 44(9), 1233–1247.

Nakashima, Y., and Watanabe, Y. (2002). "Estimate of transport properties of porous media by microfocus x-ray computed tomography and random walk simulation." *Water Resour. Res.*, 38(12), 1272.

O'Connor, R. M., and Fredrich, J. T. (1999). "Microscale flow modelling in geologic materials." *Phys. Chem. Earth A*, 24(7), 611–616.

Pham, D. L., Xu, C., and Prince, J. L. (2000). "Current methods in medical image segmentation." *Ann. Rev. Biomed. Eng.*, 2, 315–337.

Piller, M., Schena, G., Nolich, M., Favretto, S., Radaelli, F., and Rossi, E. (2009). "Analysis of hydraulic permeability in porous pedia: From high resolution x-ray tomography to direct numerical simulation." *Transp. Porous Media*, 80(1), 57–78.

Promentilla, M., Sugiyama, T., Hitomi, T., and Takeda, N. (2009). "Quantification of tortuosity in hardened cement pastes using synchrotron-based x-ray computed microtomography." *Cem. Concr. Res.*, 39(6), 548–557.

Richards, L. A. (1931). "Capillary conduction of liquids through porous mediums." *Phys.*, 1(5), 318–333.

Roels, S., and Carmeliet, J. (2006). "Analysis of moisture flow in porous materials using microfocus x-ray radiography." *Int. J. Heat Mass Tran.*, 49(25–26), 4762–4772.

Savidge, C. (2010). "Characterization of porous building materials for agent transport predictions using artificial neural networks." M.S. thesis, University of Vermont, Burlington, VT.

White, J. A., Borja, R. I., and Fredrich, J. T. (2006). "Calculating the effective permeability of sandstone with multiscale lattice boltzmann/finite element simulations." *Acta Geotech.*, 1(4), 195–209.

Willson, C. S., Stacey, R. W., Ham, K., and Thompson, K. E. (2004). "Investigating the correlation between residual nonwetting phase liquids and pore-scale geometry and topology using synchrotron x-ray tomography." *Proc. SPIE*, U. Bonse, ed., Vol. 5535, The International Society for Optics and Photonics (SPIE), Bellingham, WA, 101–111.

Zhao, W. S., and Ioannidis, M. A. (2007). "Effect of napl film stability on the dissolution of residual wetting napl in porous media: A pore-scale modeling study." *Adv. Water Resour.*, 30(2), 171–181.

J. Mater. Civ. Eng. 2013.25:1803-1812.